

Modeling of Earth's bow shock: Applications

J. F. Chapman and Iver H. Cairns

School of Physics, University of Sydney, Sydney, New South Wales, Australia

Received 14 April 2004; revised 5 July 2004; accepted 4 August 2004; published 3 November 2004.

[1] Shock-crossing data obtained from spacecraft are used to test the shock location models derived by *Chapman and Cairns* [2003]. Three sets of data are considered: (1) ISEE 1 for 24–25 September 1987, (2) Wind, Geotail, IMP 8, and Interball for the intervals 26–27 April and 10–13 May 1999, and (3) IMP 8, Geotail, Magion-4, and Cluster during the period 1973–2003 from the bow shock database (available at <http://nssdc.gsfc.nasa.gov/ftp/helper/bowshock.html>). Derived from MHD simulations, the two shock models are for angles $\theta_{\text{IMF}} = 45^\circ$ and 90° between the upstream magnetic field \mathbf{B}_{IMF} and solar wind velocity \mathbf{v}_{sw} . These models have azimuthal asymmetries, and they depend explicitly on the upstream Mach number M_A and ram pressure P_{ram} . We also test *Cairns et al.*'s [1995] rotationally symmetric shock model. The new models perform better on average than the rotationally symmetric model, providing some evidence and support for the shock's shape being strongly dependent upon M_A and θ_{IMF} . We also compare our analyses here with model/spacecraft comparisons performed by *Merka et al.* [2003a] and discuss the importance of filtering on the model predictions. **INDEX TERMS:** 2154

Interplanetary Physics: Planetary bow shocks; 2139 Interplanetary Physics: Interplanetary shocks; 7851 Space Plasma Physics: Shock waves; 2784 Magnetospheric Physics: Solar wind/magnetosphere interactions;

KEYWORDS: bow shock shape, Earth, Mach number, magnetohydrodynamics, magnetopause, modeling

Citation: Chapman, J. F., and I. H. Cairns (2004), Modeling of Earth's bow shock: Applications, *J. Geophys. Res.*, 109, A11202, doi:10.1029/2004JA010540.

1. Introduction

[2] Earth's bow shock responds to changes in solar wind conditions by varying its shape and location. These conditions are prescribed by the solar wind ram pressure P_{ram} , flow velocity \mathbf{v}_{sw} , interplanetary magnetic field (IMF) vector \mathbf{B}_{IMF} , and the Alfvén, sonic, and magnetosonic Mach numbers M_A , M_S , and M_{ms} , respectively [e.g., *Spreiter et al.*, 1966; *Fairfield*, 1971; *Farris et al.*, 1991; *Peredo et al.*, 1995; *Bennett et al.*, 1997; *Verigin et al.*, 2001; *Fairfield et al.*, 2001; *Chao et al.*, 2002; *Dmitriev et al.*, 2003]. Previously, *Chapman and Cairns* [2003] (hereinafter referred to as CC2003) analyzed shock locations derived from *Cairns and Lyon's* [1995] global three-dimensional (3-D) ideal magnetohydrodynamic (MHD) simulations. These simulations yielded sets of 3-D shock locations for IMF orientations $\theta_{\text{IMF}} = 45^\circ$ and 90° for multiple M_A and M_{ms} . From these data, shock models were developed describing the 3-D shape and location of Earth's bow shock as a function of P_{ram} , M_A , and an azimuthal angle ϕ , using both paraboloid and tilted paraboloid shape functions. These analyses show strong evidence for asymmetries in the shock's cross section perpendicular to \mathbf{v}_{sw} , consistent with the nonisotropic nature of the fast mode speed. An additional result is that the shock's symmetry axis tilts away from the nominal direction (along \mathbf{v}_{sw}) for $\theta_{\text{IMF}} = 45^\circ$ but not for $\theta_{\text{IMF}} = 90^\circ$, with these effects becoming increasingly

prevalent as $M_A \rightarrow 1$. More recently, additional simulations were performed for several IMF orientations in the ranges $20^\circ \leq \theta_{\text{IMF}} \leq 60^\circ$ and $1.4 \leq M_A \leq 9.7$ [*Chapman et al.*, 2004]. They showed that strong skewing effects were larger for lower M_A , with the shock becoming increasingly asymmetric. However, symmetry was recovered for $\theta_{\text{IMF}} = 0^\circ$ (although the nose region developed a dimple) and also as $\theta_{\text{IMF}} \rightarrow 90^\circ$. Again, these effects were qualitatively consistent with v_{ms} being nonisotropic.

[3] This paper involves the comparison of shock locations predicted by the CC2003 3-D models with three data sets. For completeness a rotationally symmetric paraboloidal model is also compared with the data, described using *Cairns and Lyon's* [1995] model for the shock standoff distance a_s and *Cairns et al.*'s [1995] model for the paraboloid flaring parameter b_s . *Merka et al.* [2003a] have recently compared IMP 8 data obtained over a 12 year period with a number of different shock models found in the literature, including the models of *Formisano* [1979], *Němeček and Šafránková* [1991], *Farris and Russell* [1994], and *Peredo et al.* [1995], as well as the rotationally symmetric paraboloidal model mentioned above [*Cairns and Lyon*, 1995; *Cairns et al.*, 1995]. We also compare our analyses here with model/spacecraft comparisons performed by *Merka et al.* [2003a] and discuss the importance of data filtering on the model predictions.

[4] The first spacecraft data set analyzed here contains 15 shock crossings observed by the ISEE 1 spacecraft during the period 24–25 September 1987 [*Cairns et al.*, 1995]. The second data set contains 14 shock crossings

observed in the intervals 26–27 April 1999 and 10–13 May 1999 by the Wind, Geotail, IMP 8, and Interball spacecraft [Fairfield *et al.*, 2001; D. H. Fairfield, personal communication, 2000]. In each of these periods the Alfvén and fast mode Mach numbers were often quite low, allowing detailed testing of the new shock models. The third data set contains observed shock crossings from the IMP 8, Geotail, Magion-4, and Cluster spacecraft for the interval 1973–2003 (bow shock database available at <http://nssdc.gsfc.nasa.gov/ftp/helper/bowshock.html>). The IMP 8 data set was also analyzed by Merka *et al.* [2003a, 2003b].

[5] This paper is set out as follows. Section 2 summarizes the new shock models developed by CC2003. In section 3, coordinate rotations are discussed, together with the methods for comparing the model predictions with data. In sections 4–7 the spacecraft data are compared with the model predictions. Section 8 discusses the results, and the conclusions are given in section 9.

2. New Shock Models

[6] The elliptical paraboloid shock models developed by CC2003 are relevant for $\theta_{\text{IMF}} = 45^\circ$ and 90° and were derived using the 3-D shock locations found in Cairns and Lyon's [1995] ideal MHD simulations. The simulations used Farris *et al.*'s [1991] average ($B_z = 0$) 3-D magnetopause model as a hard, infinitely conducting, inner boundary, with some solar wind parameters held constant ($\gamma = 5/3$, $v_{\text{sw}} = 400 \text{ km s}^{-1}$, and $M_S = 7.6$) but others allowed to vary (M_A , θ_{IMF} , and B_{IMF}). In the simulations, \mathbf{v}_{sw} lies antiparallel to the x axis, with \mathbf{B}_{IMF} lying in the x - z plane.

[7] In the $\theta_{\text{IMF}} = 90^\circ$ simulations the shock's symmetry axis remains along the x axis. There is a dependence upon an azimuthal angle ϕ measured from the z axis in the y - z plane, with the shock modeled by

$$x_m^{90^\circ} = a_s + b_{s\phi} r_\phi^2. \quad (1)$$

Here a_s is the standoff distance of the shock measured along the Sun-Earth line, and $b_{s\phi}$ and r_ϕ denote the flaring parameter and the distance to the shock (from the origin (0, 0, 0)), respectively. The standoff distance and terminator distance (measured in the y - z plane for $x = 0$) are given by [CC2003]

$$a_s = \left(\alpha_0 + \frac{\alpha_1}{M_A^2} \right) \left(\frac{P_{\text{ram}}}{1.87 \text{ nPa}} \right)^{-1/6} R_E \quad (2)$$

$$L_\phi = \left(A_\phi + \frac{B_\phi}{M_A^2} \right) \left(\frac{P_{\text{ram}}}{1.87 \text{ nPa}} \right)^{-1/6} R_E. \quad (3)$$

Here $(\alpha_0, \alpha_1) = (13.9, 32.2)$ (for the $\theta_{\text{IMF}} = 90^\circ$ model), $A_\phi = i + j|\cos\phi| + k\cos\phi^2$, $B_\phi = l + m|\cos\phi| + n\cos\phi^2$, and the fit parameters i, j, k, l, m , and n are given in Table 1 for $\theta_{\text{IMF}} = 90^\circ$. Then, $b_{s\phi}(M_A, P_{\text{ram}})$ can be written as

$$b_{s\phi} = \frac{a_s}{L_\phi^2} R_E^{-1}. \quad (4)$$

[8] The shock's symmetry axis tilts away from the $-\mathbf{v}_{\text{sw}}$ direction in the $\theta_{\text{IMF}} = 45^\circ$ simulations, requiring an

Table 1. Fit Parameters for Equation (3)

Quantity	θ_{IMF}	i	j	k	l	m	n
L_ϕ	90°	25.42	−0.82	−0.98	79.45	3.96	−9.55
$L_{\phi'}$	45°	24.55	−0.1341	−0.1341	80.147	−8.5087	−8.5087

additional dependence upon a tilt angle ψ_z measured in the x - z plane. The shock shape is generated by rotating a symmetric paraboloid

$$x_m^{45^\circ} = a'_s - b'_{s90^\circ} y^2 - b'_{s0^\circ} z^2, \quad (5)$$

through an angle ψ_z in the x - z plane. The parameters a'_s and $b'_{s\phi}$ are given by equation (2) with $(\alpha_0, \alpha_1) = (13.9, 29.0)$ and equations (3) and (4) with the parameters from Table 1 for $\theta_{\text{IMF}} = 45^\circ$. The representation of the shock surface then becomes

$$\begin{bmatrix} x_s \\ y_s \\ z_s \end{bmatrix} = \begin{bmatrix} \cos\psi_z & 0 & -\sin\psi_z \\ 0 & 1 & 0 \\ \sin\psi_z & 0 & \cos\psi_z \end{bmatrix} \begin{bmatrix} x_{45^\circ} \\ y \\ z \end{bmatrix}. \quad (6)$$

Here ψ_z is given by

$$\psi_z = (7.0 - 0.74M_A)^\circ. \quad (7)$$

Equation (7) is only valid in the range $1 < M_A < 9.7$, since this empirical relation is derived from the CC2003 simulations which only explored this parameter range. For $M_A > 9.7$ one would expect that $\psi_z \sim 0^\circ$ since the shock is blown back onto the magnetopause obstacle.

[9] For comparison, Cairns *et al.*'s [1995] model for b_s only includes a functional dependence upon P_{ram} :

$$b_s(P_{\text{ram}}) = 0.0223 \left(\frac{P_{\text{ram}}}{1.8 \text{ nPa}} \right)^{1/6} R_E^{-1}, \quad (8)$$

and the resulting shock is a surface of revolution with a circular cross section. Cairns and Lyon [1995] found an expression for a_s based on the density jump X at the shock:

$$\frac{a_s}{a_{mp}} = 3.4 X(M_A, \theta_{\text{IMF}}, M_S) + 0.4, \quad (9)$$

where a_{mp} denotes the magnetopause standoff distance. We use the analytic expression for the density jump X derived by Grabbe and Cairns [1995]. A rotationally symmetric shock model is compared with the ϕ -dependent models below, using Cairns *et al.*'s [1995] model for b_s with Cairns and Lyon's [1995] model for a_s . In equation (9), values of a_{mp} are taken from the magnetopause model of Shue *et al.* [1997]. This model is also used by Merka *et al.* [2003a], allowing a more accurate comparison with their IMP 8 shock-crossing analysis. We discuss the importance of the magnetopause model in section 8.

3. Rotations and Methods of Testing

[10] All spacecraft trajectory data are originally obtained in GSE coordinates. To account for aberration due to Earth's

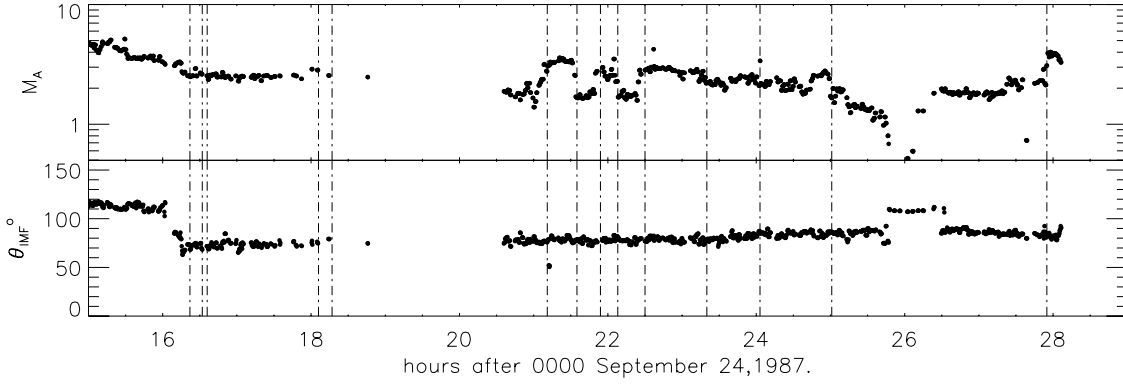


Figure 1. Alfvén Mach number M_A and θ_{IMF} as measured by the IMP 8 spacecraft during 24–25 September 1987. Dash-dotted vertical lines indicate times of the ISEE 1 spacecraft crossings.

orbital motion around the Sun, 29.8 km s^{-1} is removed from the GSE y component of the solar wind velocity \mathbf{v}_{sw} . To test the models against observed bow shock crossings, the spacecraft positions are rotated into a coordinate system in which the new x axis lies along the solar wind vector and the new z axis is defined so that \mathbf{B}_{IMF} lies in the x - z plane. This system is defined using the observed solar wind conditions and IMF vectors and is identical to the coordinate system in the simulations of Cairns and Lyon [1995] and Chapman *et al.* [2004], as well as in the CC2003 models presented in section 2.

[11] Spacecraft observations yield the proton number density n_p , the solar wind speed $v_{\text{sw}} = (v_{\text{px}}^2 + v_{\text{py}}^2 + v_{\text{pz}}^2)^{1/2}$ defined by the protons, and $B_{\text{IMF}} = (B_x^2 + B_y^2 + B_z^2)^{1/2}$ as a function of time. These parameters allow computation of the Mach numbers and ram pressure of the solar wind after the number fraction of alpha particles is assumed. On average, the relative alpha particle abundance, n_α/n_p , is 4% for the solar wind [e.g., Slavin and Holzer, 1981; Yermolev and Stupin, 1997]. This abundance is assumed in sections 4–6, and the Alfvén Mach number and ram pressure are given by $M_A = v_{\text{sw}} \sqrt{1.16 \rho_m \mu_0 / B_{\text{IMF}}}$ and $P_{\text{ram}} = 1.16 \rho_m v_{\text{sw}}^2$, where the mass density $\rho_m = n_p m_p$ denotes the mass density of the solar wind protons.

[12] To test the shock models, the observed solar wind parameters P_{ram} , M_A , and θ_{IMF} are used to predict the $x_m^{\theta_{\text{IMF}}}$ coordinate of the shock using the rotated spacecraft coordinates y_{sc} and z_{sc} . Here $x_m^{45^\circ}$ and $x_m^{90^\circ}$ represent the x coordinates predicted by the $\theta_{\text{IMF}} = 45^\circ$ (equations (5), (6), and (7)) and $\theta_{\text{IMF}} = 90^\circ$ models (equations (1), (2), and (4)), respectively. The $x_m^{\theta_{\text{IMF}}}$ coordinates of each model are compared with the spacecraft coordinate x_{sc} at the times of the shock crossings. For a model to accurately predict the shock location the x_{sc} coordinate of the spacecraft must coincide with the model's predicted x coordinate. The prediction x_i for a circular cross-sectional paraboloid with Cairns *et al.*'s [1995] model (8) for $b_s(P_{\text{ram}})$, which does not include the effects of M_A or ϕ , is also calculated and used with the prediction (9) for a_s .

[13] In comparing the $\theta_{\text{IMF}} = 45^\circ$ model the correct orientation is important. In the simulations the $\theta_{\text{IMF}} = 45^\circ$ model applies when $B_x B_z > 0$. When $B_x B_z > 0$, the shock tends to flatten over the $(+x) - (+z)$ quadrant, extending farther in the $(+x) - (-z)$ quadrant. When $B_x B_z < 0$, the model has to be reflected in the x - z plane about the x axis

(or, equivalently, setting $z_{\text{sc}} = -z_{\text{sc}}$) when comparing with data.

4. ISEE 1 24–25 September 1987 Observations

[14] The bow shock crossed the ISEE 1 spacecraft multiple times during the period 24–25 September 1987. Plots of all the solar wind data are given by Cairns *et al.* [1995]. Figure 1 shows M_A and θ_{IMF} as a function of time. Data gaps exist between hours 4 and 12 and between hours 18 and 20. IMP 8 solar wind data are used to calculate the solar wind parameters at the times of the ISEE 1 shock crossings. The IMP 8 data have been time lagged by 5.6 min to allow for convection to ISEE 1. The Alfvén Mach number was low ($1 < M_A < 3$) throughout the period with $50^\circ < \theta_{\text{IMF}} < 90^\circ$.

[15] The model predictions for the ISEE 1 shock crossings throughout 24–25 September 1987 are shown in Figure 2. The models represented by the symbols $x_m^{45^\circ}$, $x_m^{90^\circ}$, and x_i are described in section 2 and in the caption of Figure 2. The spacecraft trajectories and model predictions are smoothed using a 7.5 min centered running average. For a model to accurately predict the shock location the model trace must cross the spacecraft trajectory x_{sc} at the time of the spacecraft crossing, denoted by the vertical dash-dotted line. There are two ways of measuring differences between the model predictions and observations. The first is to look at the difference between the predicted coordinates and the spacecraft coordinates at the time of the shock crossing, i.e., $x_m^{\theta_{\text{IMF}}} - x_{\text{sc}}$. Alternatively, one can look at the difference in time between the observed and predicted shock crossing.

[16] The $x_m^{45^\circ}$ and $x_m^{90^\circ}$ models predict the first ISEE 1 crossing (hour 2.75 in Figure 2, top left) within $1 R_E$ at the time of the crossing, and the prediction lines cross the spacecraft trajectory within 3 min. The x_i model prediction, however, only comes within $1 R_E$ of the spacecraft x_{sc} coordinate at the time of the crossing and then places the spacecraft upstream of the shock between hours 2.8 and 3.5. The $x_m^{\theta_{\text{IMF}}}$ models do, however, mispredict a skimming crossing near hour 2.2. Plausibly, the spacecraft was very close to the shock at this time.

[17] The crossing near hour 16.4 is predicted early by ~ 10 min by the $x_m^{45^\circ}$ and $x_m^{90^\circ}$ models and by ~ 20 min by the x_i model (Figure 2, top right). The two crossings at hours 16.5 and 16.6 are predicted qualitatively, but the quantita-

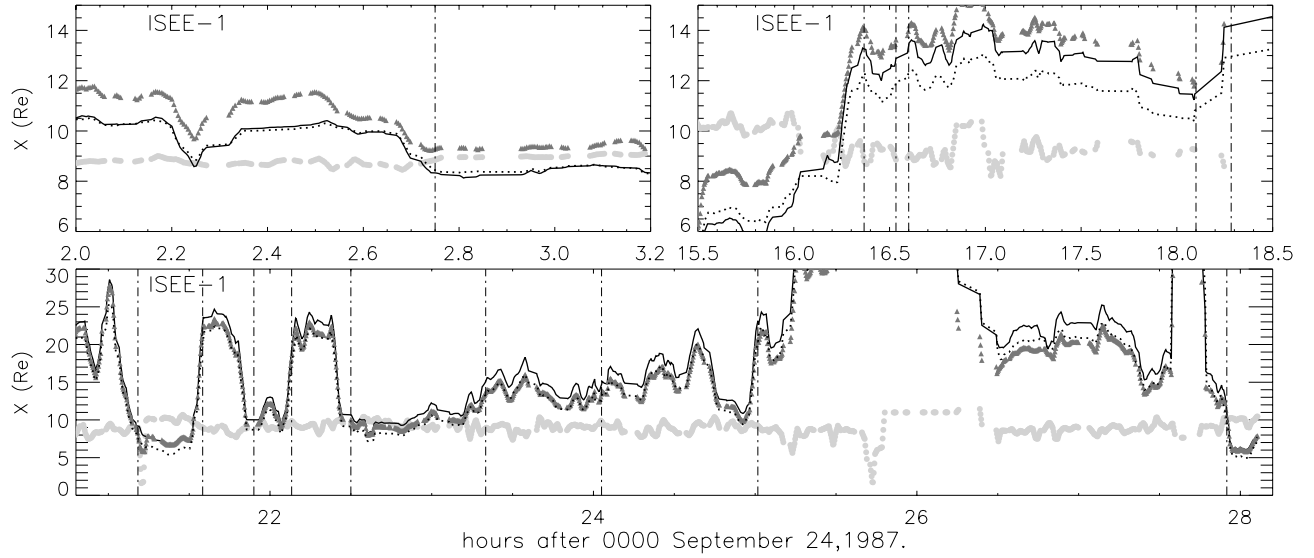


Figure 2. Model predictions for the ISEE 1 spacecraft. Light grey data points are the spacecraft x_{sc} coordinate. The dotted and solid lines are the $x_m^{90^\circ}$ and $x_m^{45^\circ}$ model predictions, respectively. The x_i model is shown in dark grey (triangles). Dash-dotted vertical lines indicate the times of the spacecraft's shock crossing.

tive differences are significant: They are predicted within $\sim 3 R_E$ for $x_m^{90^\circ}$ and $\sim 5 R_E$ for the other two models. The discrepancies for these three crossings may be primarily a timing issue: Shifting the timelines to the right by 10 min leads to better prediction for the hour 16.4 crossing and places the next two crossings on either side of dips in the prediction line around hour 16.45. It is important that the shock models used here apply to equilibrium positions of the shock and so do not include the time lags due to the shock's finite propagation speed to its new equilibrium position. This time lag Δt is composed of three parts: the time $\Delta t_{sw} = \Delta x / v_{sw}$ for the change in the solar wind parameters to convect a distance Δx from the spacecraft to the shock, the time $\Delta t_{ms,1} = (a_s - a_{mp}) / v_{sw,d}$ for the solar wind change to reach the magnetopause at the shocked solar wind speed $v_{sw,d}$, and the time $\Delta t_{ms,2} = \Delta_{ms,new} / (v_{ms} - v_{sw,d})$ for information to propagate back upstream (against the flow at $v_{sw,d}$) to the new shock location at the fast mode speed v_{ms} :

$$\Delta t = \Delta t_{sw} + \Delta t_{ms,1} + \Delta t_{ms,2}. \quad (10)$$

The solar wind speed was $\sim 390 \text{ km s}^{-1}$ between hours 16 and 17, and assuming that $\Delta x \approx 3 R_E$, $a_s - a_{mp} \approx 4 R_E$, $\Delta_{ms,new} \approx 8 R_E$, $v_{sw,d} = 200 \text{ km s}^{-1}$, and $v_{ms} \approx 300 \text{ km s}^{-1}$, then $\Delta t \approx (0.8 + 2.1 + 8.2) \text{ min} = 11.3 \text{ min}$.

[18] Thus a time lag of the order $10 \pm 5 \text{ min}$ is expected because of the finite propagation and response speeds, with longer lags plausible at lower M_A . Moreover, the 7.5 min smoothing of the data may also contribute slightly to the overpredictions, removing biases toward lower predictions. Finally, the rapid in-out nature of crossings near hours 16.5 and 16.6 and the relatively small changes in the predicted shock location for the observed solar wind conditions are qualitatively not inconsistent with a slow response and therefore slow upstream propagation speed for the shock. That is, it will take some time for the shock to physically

reach its new equilibrium position in response to changes in the solar wind. In summary, these two effects can semi-quantitatively explain the overpredictions of the shock models for these data. Additional discussion of the time lags and mispredictions is given in sections 8.1 and 8.2.

[19] There are very limited data for the two crossings at hours 18.1 and 18.3, thereby precluding detailed analysis at these crossings. However, the few data points available suggest that the model predictions move down toward and then away from the prediction line, not qualitatively inconsistent with the data.

[20] The first five crossings of the period hours 20–30 (Figure 2, bottom), at hours 21.2, 21.6, 21.9, 22.1, and 22.5, are predicted within 6 min by all models. The traces of the x_i and $x_m^{45^\circ}$ models lie on the spacecraft x_{sc} data between hours 22.5 and 23.3, mispredicting the location of the shock. However, the shock may have been very close to the spacecraft throughout this period. The $x_m^{90^\circ}$ model does a little better (as expected, since $\theta_{IMF} = 80^\circ$), placing the shock earthward of the spacecraft for the period hours 22.5–23, before coinciding with the x_{sc} coordinate between hours 23 and 23.2. The crossings at hours 24.05 and 25 are predicted within $3 R_E$ and $\sim 10 \text{ min}$, respectively, by all three models. The last crossing at hour 28 is well predicted by all the models.

5. Observations on 26–27 April 1999

[21] The solar wind parameters measured by the Wind and IMP 8 spacecraft are shown in Figure 3 for the period 26–27 April 1999. Small measured densities throughout this interval produced low values of $M_A \rightarrow 1$. The IMF orientation stayed at $\theta_{IMF} \sim 90^\circ$ around the times of the shock crossings. These data (as well as those in section 6 below) are also discussed in detail by Fairfield *et al.* [2001]. A helium to hydrogen ratio of 4% was assumed because of the Wind alpha data being unreliable for this period

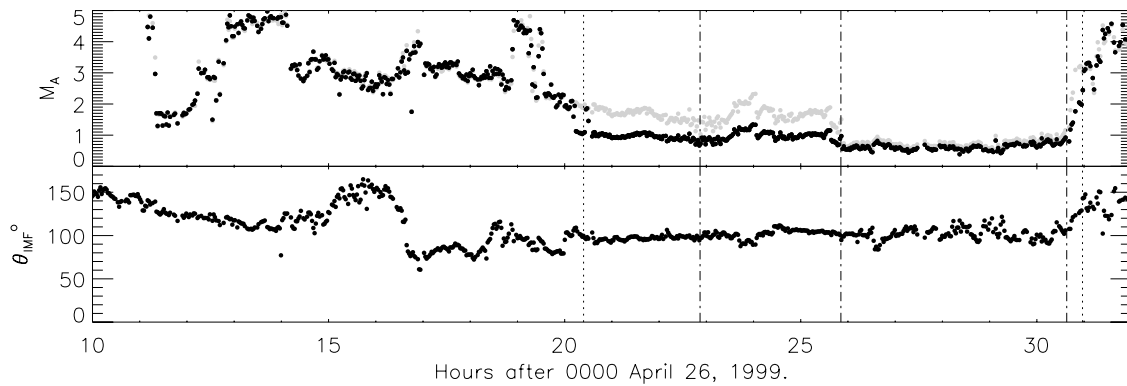


Figure 3. Alfvén Mach number M_A and θ_{IMF} calculations from IMP 8 and Wind data during 26–27 April 1999. Dotted vertical lines indicate times of the IMP 8 spacecraft crossings, while dash-dotted lines indicate the Wind crossings. Black data points in the top panel indicate measurement by IMP 8, and grey data points indicate measurement by Wind.

(J. Kasper, private communication, 2001). The rotated trajectory coordinates x_{sc} for Wind and IMP 8 are plotted in Figure 4 (using a 15 min running average to reduce the scatter), along with the model predictions. The IMP 8 shock crossings (Figure 4a) occurred at hours 20.4 and 31.0 at the rotated coordinates $(33.4, 4.8, 3.9) R_E$ and $(34.5, 8.7, -4.0) R_E$, respectively. All crossings are therefore close to the nose of the shock. All the models predict the IMP 8 shock crossings at hours 20.4 and 30.8 within 20 and 2 min, respectively. However, all three models predict multiple crossings around hour 11.5 which were not observed by the spacecraft. Comparing with Figure 3, it is clear that $M_A = 1.7$ and $\theta_{\text{IMF}} = 54^\circ$, so that neither of the $x_m^{\theta_{\text{IMF}}}$ models are exactly appropriate. Noting that the Wind and IMP 8 data predict modestly different values of M_A , and so shock positions, the mispredictions may be due to measurement issues, fronts of changing solar wind quantities being neither nonplanar nor aligned with the x axis, or (less plausibly) time lag effects. These possibilities are discussed more in sections 6 and 8.

[22] The Wind shocks occurred at hours 25.9 and 30.6 (Figure 4b) at the rotated coordinates, ordered by time, of $(38.5, -20.6, -26.0) R_E$ and $(44.9, -8.0, -24.4) R_E$, respectively. A transitory pair of crossings, in which the Wind spacecraft moved across the shock and back again in

2 min, occurred at hour 22.9, when Wind was at the rotated coordinates $(38.9, -11.4, -29.6) R_E$. The $x_m^{45^\circ}$ and $x_m^{90^\circ}$ models predict the time between these crossings near hour 22.9 as 15 min (of order of smoothing time); the x_i model predicts these within ~ 3 min. The last two Wind crossings are predicted accurately by all models. Although $\theta_{\text{IMF}} \sim 90^\circ$ throughout the times of the IMP 8 and Wind crossings, there are few significant differences between the predictions of $x_m^{45^\circ}$ and $x_m^{90^\circ}$. This lack of observable differences in the models (e.g., $x_m^{45^\circ}$ versus $x_m^{90^\circ}$) is expected since all spacecraft were well upstream of the Earth and $a_s(P_{\text{ram}}, M_A)$ is very similar for both models.

6. Observations on 10–13 May 1999

[23] Figure 5 shows M_A and θ_{IMF} , measured by the Solar Wind Experiment and Magnetic Field Experiment instruments on board the Wind spacecraft, as a function of time for the period 10–13 May 1999. As mentioned in section 5, these data are discussed in detail by *Fairfield et al.* [2001]. Throughout this period, $v_{sw} \sim 400 \text{ km s}^{-1}$, low densities led to low measured values of M_A , and θ_{IMF} lies between 10° and 90° at the times of the crossings. The data are smoothed using a 15 min running average. It is noted that there is a data gap between hours 44 and 47.

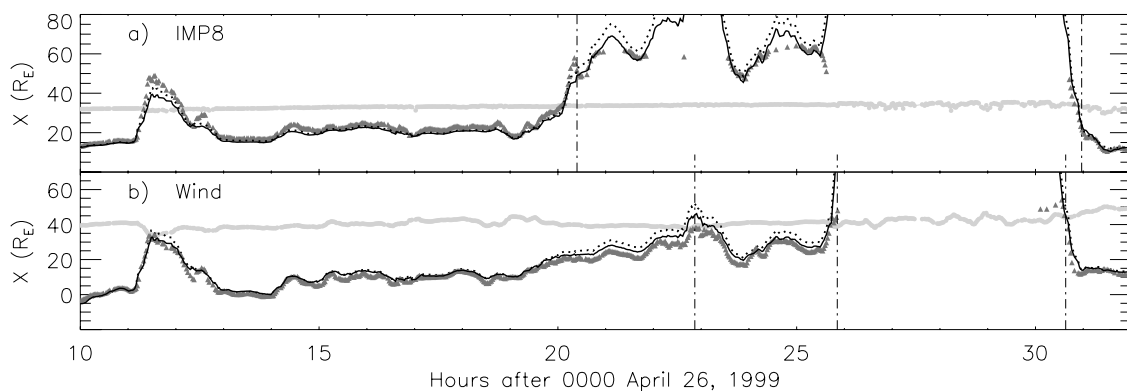


Figure 4. Model predictions for the (a) IMP 8 and (b) Wind spacecraft during the period 26–27 April 1999. The line/data point series are the same as in Figure 2.

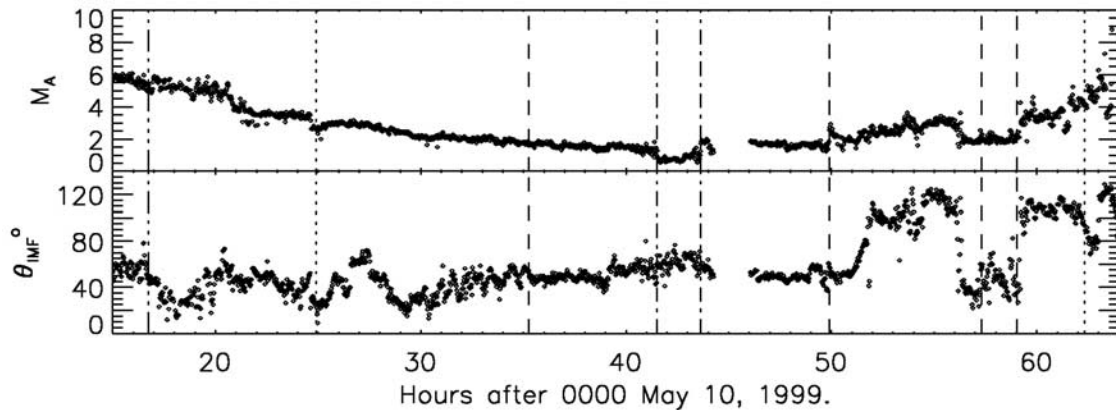


Figure 5. Alfvén Mach number M_A and θ_{IMF} as measured by the Wind spacecraft during 10–13 May 1999. Dotted, dashed, dash-dotted, and dot-dot-dot-dashed vertical lines indicate crossings by the Interball, IMP 8, Wind, and Geotail spacecraft, respectively.

[24] Figure 6 shows the model predictions for the Wind and Geotail spacecraft. The rotated spacecraft coordinates x_{sc} and the model predictions are smoothed using a 15 min running average to reduce the scatter. At hour 16.75 (after 0000 UT on 10 May), Geotail crossed the bow shock at coordinates (6.6, -6.2 , 25.0) R_E . At this time, Wind measures $M_A = 5.3$ and $\theta_{\text{IMF}} = 50^\circ$. All three models predict the Geotail shock-crossing location within 1 R_E at the time of the crossing. However, the x_i model trace lies on the spacecraft x_{sc} for the first 8 hours, mispredicting shock crossings throughout this period. The $x_m^{\theta_{\text{IMF}}}$ model traces also lie close to x_{sc} , suggesting that the spacecraft may have been very close to the shock between hours 1 and 8.

[25] The two shock crossings observed by the Wind spacecraft at hours 41.5 and 43.6 are shown in Figure 6b. At hours 41.5 and 43.6 the spacecraft has the rotated coordinates (32.2, 23.1, -34.4) R_E and (30.3, 4.5, -43.1) R_E , with $M_A = 1.4$ and 1.8 and $\theta_{\text{IMF}} = 52^\circ$ and 56° , respectively. All three models predict the shock crossing too early, near hour 37. *Fairfield et al.* [2001] gave similar discrepancies for this crossing, attributing them to unreliable density data obtained by Wind preceding the crossing when Wind was inside the foreshock. As well as this, the measured densities are so low, $\sim 0.2 \text{ cm}^{-3}$ with $M_A \sim 1.3$, that the model predictions are very sensitive to small

changes in density, implying that the large overpredictions may be due to experimental problems, not problems with the models.

[26] All three models accurately predict the second Wind shock crossing at hour 43.6. The lack of data after the crossing at hour 43.6 makes it impossible to determine where the models place the shock. All models incorrectly predict the shock moving over the spacecraft at hours 48 and 50.

[27] Figure 7 compares the models with the Interball and IMP 8 shock crossings. For the Interball crossings the spacecraft was at the rotated coordinates (19.2, 14.6, 0.0) R_E and (16.2, -4.3 , 1.5) R_E at hours 24.9 and 62.3, with $M_A = 2.9$ and 4.0 and $\theta_{\text{IMF}} = 27$ and 94, respectively. The first Interball crossing is predicted early at hour 22, not inconsistent with the simulations showing smaller a_s for smaller θ_{IMF} [*Chapman et al.*, 2004]. The second crossing is predicted within 1 R_E by all models. During this crossing, no large differences exist between the models since we are at the nose of shock, and we can only expect to observe small differences in the predicted values for a_s .

[28] The four IMP 8 crossings (Figure 7b) occurred at hours 35.3, 49.9, 57.3, and 59.0 when $M_A = 1.6$, 2.5, 2.0, and 2.0 and $\theta_{\text{IMF}} = 54.6$, 57.5, 55.8, and 42.2, respectively.

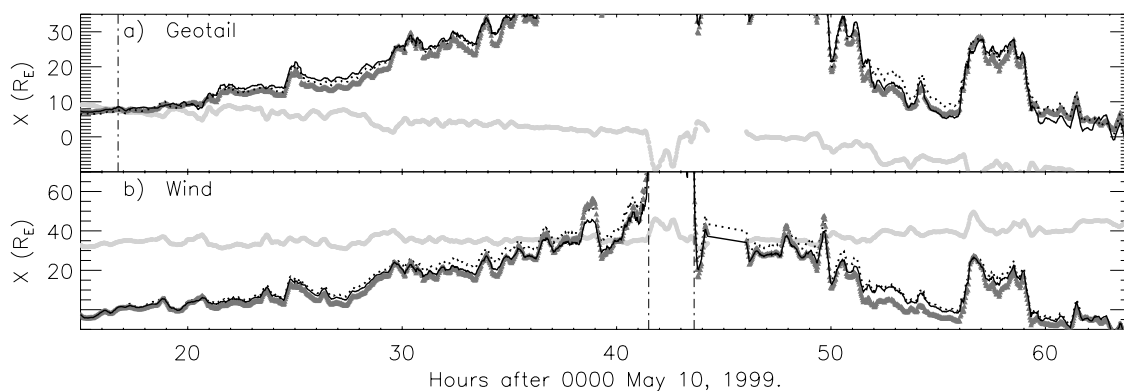


Figure 6. Model predictions for the (a) Geotail and (b) Wind spacecraft during the period 10–13 May 1999. The line/data point series are the same as described in the caption for Figure 2.

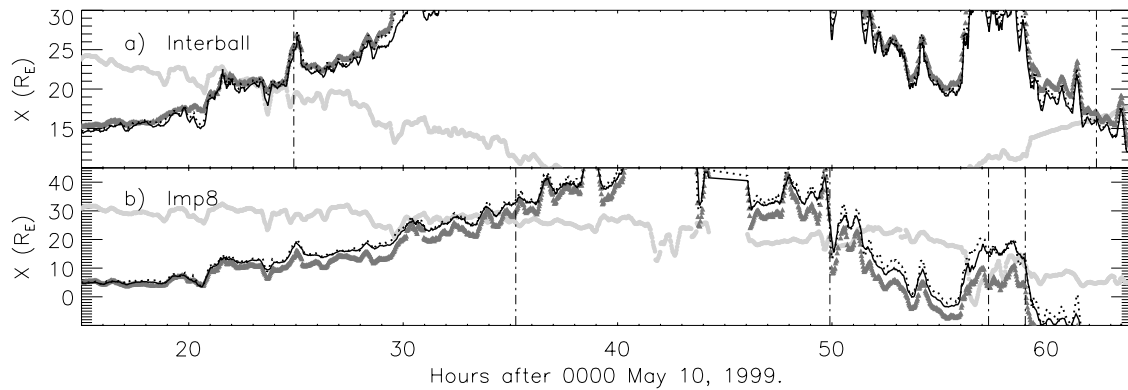


Figure 7. Model predictions for the (a) IMP 8 and (b) Interball spacecraft during the period 10–13 May 1999. The line/data point series are the same as in Figure 2.

The rotated coordinates of the four shock crossings, in order of increasing time, are $(25.9, -18.3, 28.2) R_E$, $(20.3, -31.6, 20.8) R_E$, $(22.1, 7.1, 36.1) R_E$, and $(6.3, -32.9, -26.8) R_E$. The predictions of $x_m^{90^\circ}$, $x_m^{45^\circ}$, and x_i all overpredict the first crossing (hour 35.3) by a considerable amount, first crossing the spacecraft line at hour 32 (3.3 hours early). The measured density and Mach number for this crossing are low ($n_{sw} = 0.34 \text{ cm}^{-3}$, $M_A \sim 1.67$, and $M_S = 5.7$), as they are also in the 2–3 hours preceding the crossing. This suggests again that the reason for the misprediction is the high sensitivity of the models for small M_A and n_{sw} . As well as this the shock was moving outward, implying that the equilibrium position could be farther out (larger x coordinate) than that observed. The model predictions are for static or equilibrium positions of the shock, and since the shock itself is moving, this difference could explain some of the discrepancy between the predicted and observed shock location.

[29] The second IMP 8 shock crossing, caused by a sudden inward motion, is well predicted by the $x_m^{90^\circ}$ and $x_m^{45^\circ}$ models, as shown by the model lines dipping rapidly to cross the trajectory at hour 49.9. However, the models mispredict a crossing at hour 52, and the crossing at hour 57.3 is predicted too early but within 1 hour of the observed crossing. *Fairfield et al.* [2001] obtain similar time discrepancies, attributing this to spatial variations in the solar wind between the IMP 8 and Wind spacecraft, which could cause a misprediction of 1 hour at Wind. The last crossing is predicted accurately by the $x_m^{45^\circ}$ and $x_m^{90^\circ}$ models. The x_i model with $b_s = b_s(P_{ram})$ only works well for the first three IMP 8 crossings and does not predict the last crossing (x_i lies below the IMP 8 trajectory line). This model also mispredicts crossings between hours 42 and 47.

7. Bow Shock Database Data

[30] In this section we present shock data obtained from the online bow shock database (available at <http://nssdc.gsfc.nasa.gov/ftp/helper/bowshock.html>). The observational periods for the data sets are as follows: 1973–2000 for IMP 8, 1996–1997 for Magion-4, 2001–2002 for Cluster, and 1995–1997 for Geotail. The solar wind parameters are available for each specific spacecraft, appropriate for testing with the shock models. The IMP 8 database has additional observational flag parameters, and only those shock cross-

ings are selected which are unambiguous in all the available data and where all required data are available. All data have been filtered with $300 \text{ km s}^{-1} < v_{sw} < 500 \text{ km s}^{-1}$, $1 < M_A < 10$, and $4 < M_S < 10$. These filters led to 648 crossings by IMP 8, 210 by Magion-4, 227 by Cluster, and 145 by Geotail.

[31] By analogy with the analyses by *Merka et al.* [2003a], in Figure 8 we show the ratio R_{model}/R_{obs} , where $R_{model} = \sqrt{x_m^2 + y_m^2 + z_m^2}$ and $R_{obs} = \sqrt{x_{sc}^2 + y_{sc}^2 + z_{sc}^2}$ are the distance of the shock from Earth as given by the model predictions and measured by the spacecraft, respectively. For each spacecraft the ratios were obtained by binning the data into intervals of θ_{IMF} and then averaging over all values of R_{model}/R_{obs} in that bin for each model. A ratio of 1 implies a perfect prediction on average with $R_{model} = R_{obs}$, and we have plotted a horizontal dotted line at $R_{model}/R_{obs} = 1$.

[32] On average the $x_m^{\theta_{IMF}}$ models do very well for all four spacecraft with $1 < |R_{model}/R_{obs}| < 1.058 \pm 0.002$ for the range $40^\circ < \theta_{IMF} < 140^\circ$ where these models are appropriate. More specifically, the $x_m^{\theta_{IMF}}$ models are only in error by 2% for IMP 8 (for $60^\circ < \theta_{IMF} < 140^\circ$), 5% for Geotail and Cluster, and 2% for Magion-4. Outside this range the model predictions worsen on average, which is to be expected since the models are outside their domain of applicability and asymmetries in the shock increase as θ_{IMF} decreases ($20^\circ < \theta_{IMF} < 40^\circ$ and $140^\circ < \theta_{IMF} < 180^\circ$) [*Chapman et al.*, 2004]. Differences exist in the predictive capabilities of the x_i and $x_m^{\theta_{IMF}}$ models in the Magion-4 and Cluster results. For example, the x_i model overestimates the shock locations by up to 20% of the Cluster data for the $80^\circ < \theta_{IMF} < 100^\circ$ bin, whereas the $x_m^{\theta_{IMF}}$ models are within 4% of a perfect prediction. Similar comparisons can be made in the other θ_{IMF} bins, as well as in the Magion-4 data, with the x_i model doing worse on average.

[33] Figure 9 shows similar comparisons in which the shock crossings are separated into M_A bins. Here the $x_m^{\theta_{IMF}}$ models are only in error by 7% for IMP 8, 6% for Magion-4, 4% for Geotail, and 6% for Cluster (but only in the range $4 < M_A \leq 10$). Again, the x_i model shows larger differences than the other models between the observed and predicted values for the Magion-4 and Cluster spacecraft.

[34] Differences between the predictive capabilities of the $x_m^{45^\circ}$ and $x_m^{90^\circ}$ models are not obvious in Figures 8 and 9. To observe the geometric effects predicted for the models (seen in the simulations of *Chapman et al.* [2004]), such as the

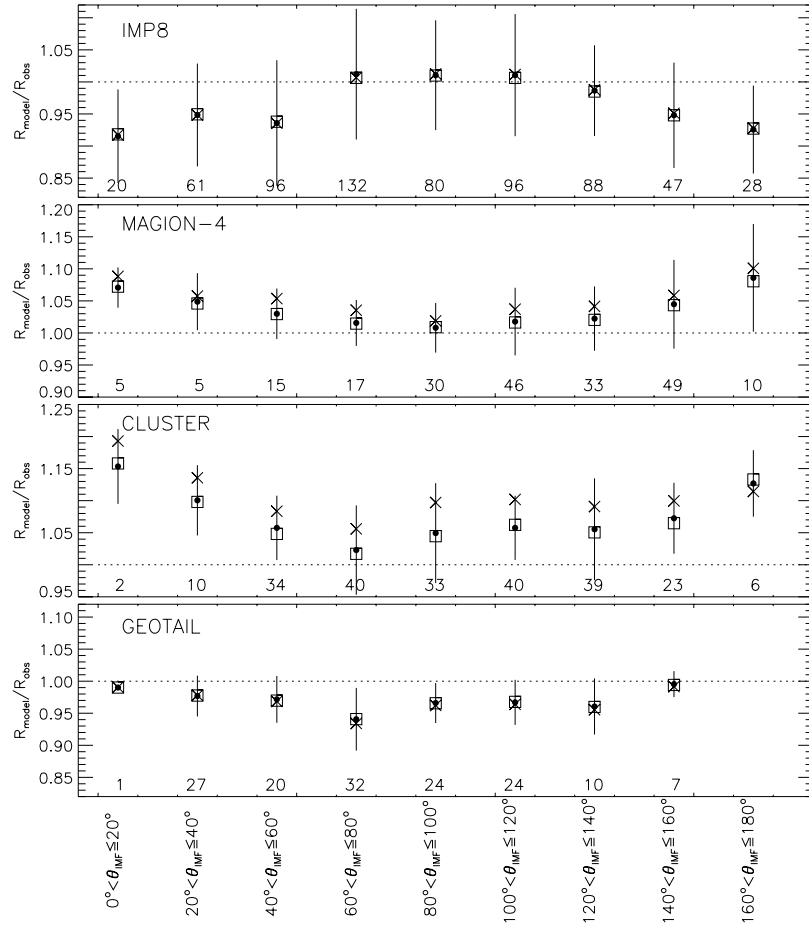


Figure 8. Ratio $R_{\text{model}}/R_{\text{obs}}$ is plotted for each spacecraft from the filtered bow shock database in bins of θ_{IMF} . The three models $x_m^{45^\circ}$, $x_m^{90^\circ}$, and x_i are plotted using squares, circles, and crosses, respectively. The standard errors of the mean are plotted for the $x_m^{90^\circ}$ model, with the other two models having similar standard errors. The numbers along the bottom of each plot window indicate the number of shock crossings in each bin.

tilting or flattening of the shock in x - z planes for the $x_m^{45^\circ}$ model in contrast to the shock's symmetric shape in the $x_m^{90^\circ}$ model, the shock crossings need to be observed in specific planes. For instance, in the y - z plane the shock should be flattened over the $+z$ quadrants for oblique IMF, and noncircular cross sections are expected for all θ_{IMF} [Chapman *et al.*, 2004]. One problem with this is that multiple shock crossings are required for low enough M_A where these effects are prominent and easily observed. Only the IMP 8 database contains enough crossings for statistically significant analyses to be performed. In Figure 10 the IMP 8 shock-crossing coordinates (y_{sc} , z_{sc}) are plotted for $M_A < 5$, $\theta_{\text{IMF}} < 80^\circ$, $\theta_{\text{IMF}} > 100^\circ$, and spacecraft locations $-10 R_E < x_{sc} < 12 R_E$, regimes where tilting or skewing of the shock is possible [Chapman *et al.*, 2004; CC2003]. These restrictions leave 56 shock crossings. In this data set, 6% of the data have $M_A < 3$, and the other 94% are in the range $3 < M_A < 5$. The fit in Figure 10 shows a shifted ellipse, in analogy with Figure 8 of CC2003, of the form $Y^2/A^2 + (z + z_0)^2/B^2 = 1$. The fit was performed with free parameters A , B , and z_0 , yielding a shift in the cross section along z of $-2.6 \pm 0.52 R_E$ (i.e., $z_0 = -2.6 \pm 0.52 R_E$). This is consistent with the shock models which predict a shift

in the z coordinate of the centroid in the range 1.8 – $4.8 R_E$ for $2 < M_A < 5$ (see CC2003, Figure 8).

[35] To test for $b_{s\phi}$ effects (or elliptical cross-sectional effects), the IMP 8 data for $5 < M_A < 10$ are shown in Figure 11. A nonshifted elliptical fit to the data of the form $Y^2/A^2 + z^2/B^2 = 1$ has the semimajor axis lying along the y axis and is $4.5 \pm 0.9\%$ larger ($L_z/L_y = 0.92$) than the semiminor axis along z . This implies an eccentricity of 0.4, consistent with those observed in the simulations of CC2003 for $M_A \sim 5$ (see CC2003, Figure 7). These two effects, the shift of the centroid of the cross section for $2 < M_A < 5$ and the noncircular cross sections for $5 < M_A < 10$, are both qualitatively and quantitatively consistent with the results of CC2003 and Chapman *et al.* [2004] (see also the discussion in section 8.3).

8. Discussion

8.1. Time Lag Effects

[36] The shock models describe the equilibrium positions of the shock, but the shock crossings in sections 4–6 are measured as the shock moves over the spacecraft (any movement of the spacecraft is negligible compared with

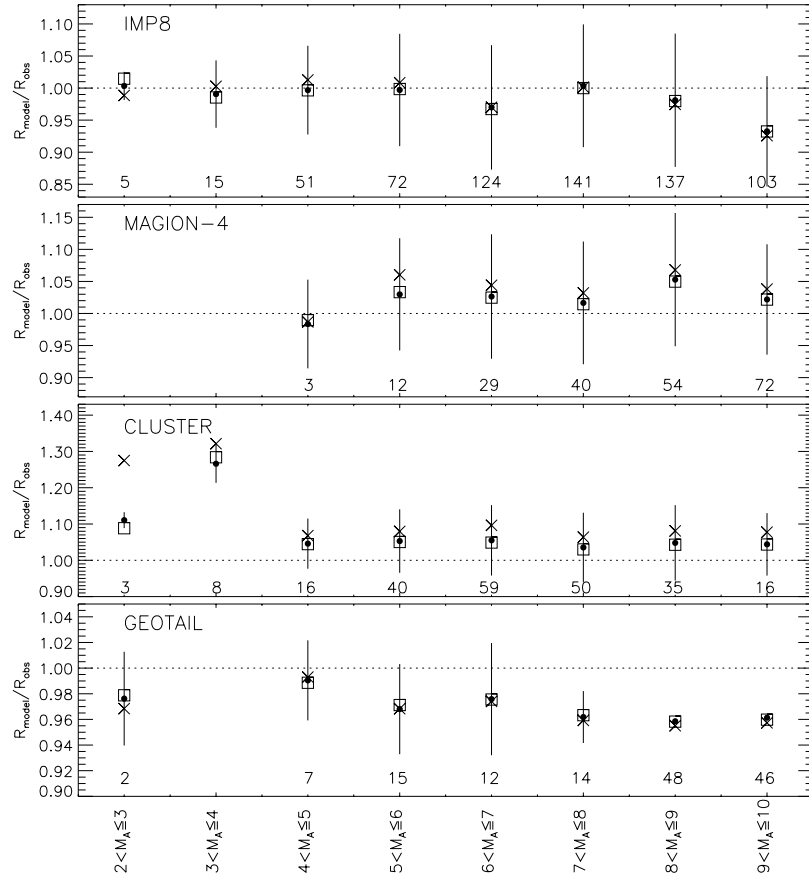


Figure 9. Ratio $R_{\text{model}}/R_{\text{obs}}$ for each spacecraft, binned in M_A , for the filtered bow shock database. The symbols are the same as in Figure 8.

the timescales for the movement of the shock). This implies that the equilibrium positions of outbound and inbound shocks passing over the spacecraft are farther from and closer to Earth, respectively, than the measured spacecraft

crossing. Table 2 summarizes the shock crossings of sections 4–6 indicating the nature of each crossing as either outbound or inbound. Relationships between the timing of the crossings are clear: Almost all (12 of 13) outbound

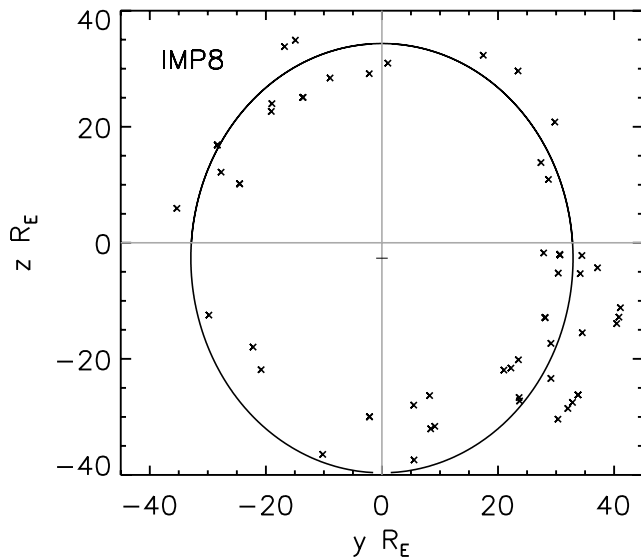


Figure 10. IMP 8 y and z shock crossing coordinates for $M_A < 5$ and $-10 R_E < x_{sc} < 12 R_E$. The solid line is a shifted elliptical fit. The horizontal line on the y axis shows the center of the ellipse.

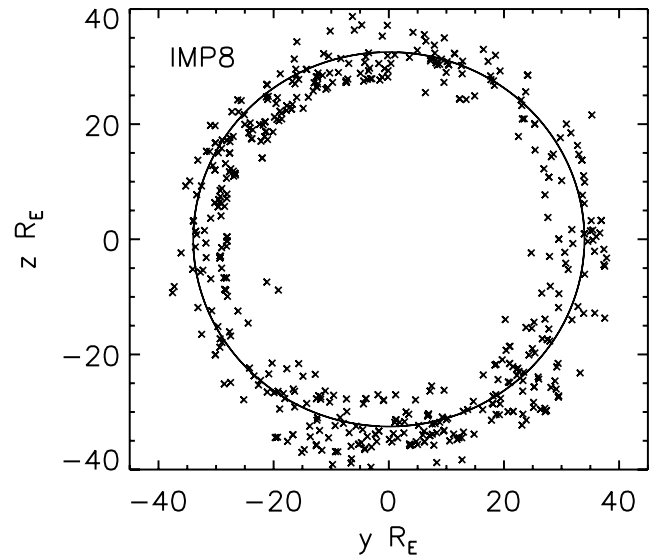


Figure 11. IMP 8 y and z shock crossing coordinates for $5 < M_A < 10$ and $-10 R_E < x_{sc} < 12 R_E$. The solid line is an elliptical fit.

Table 2. Summary of Shock Crossings in Sections 4 and 6

Figure	Spacecraft	Number of Crossings	Early		On Time	
			Outbound	Inbound	Outbound	Inbound
2	ISEE 1	10	5	1	0	4
4	IMP 8	2	1	0	0	1
4	Wind	3	2	0	0	1
6	Geotail	1	0	0	1	0
6	Wind	2	1	0	0	1
7	Interball	2	1	0	0	1
7	IMP 8	4	2	0	0	2
Total		24	12	1	1	10

crossings are early, and almost all (10 of 11) inbound crossings are on time. The only on-time outbound crossing was for the high M_A (~ 5.5) Geotail crossing at hour 16.75 (10–13 May 1999). There is a clear correlation in Table 2: Early model predictions are produced for outbound, low M_A shocks, and the on-time predictions occur for inbound shocks. This can be explained qualitatively in terms of the time lags for the propagation of information from the solar wind to the magnetopause and then back upstream to the shock, as described in equation (10). For an outbound shock the time lag should be larger for lower M_A , since the propagation distances for which the information must travel become greater (e.g., Δ_{ms} increases as M_A decreases) and the relative speed $(v_{ms} - v_{sw,d})/v_{sw}$ becomes smaller. For inbound shocks, in contrast, the shock plausibly moves to its new equilibrium position at v_{sw} in a time $\approx \Delta x/v_{sw}$.

8.2. Systematic Effects

[37] The $x_m^{\theta_{IMF}}$ and x_i models describe the equilibrium position of the shock and do not include several effects. First, they do not take into account the finite propagation speed of the shock. The solar wind conditions at any given time are used in the models to predict the instantaneous location of the shock; however, it will take time for the shock to physically reach its new equilibrium position. So, for example, the early prediction of an outward moving shock (due to M_A or P_{ram} decreasing, e.g., or θ_{IMF} changing), or the late prediction of an inward moving shock, is potentially due to the finite time required for the shock to reach the new equilibrium position. The early predictions of the outbound crossings in sections 4–6, for example, the multiple ISEE 1 crossings in Figure 2 (hours 16.4, 21.6, 22.1, and 25.0) and the first IMP 8 crossing at hour 35.3 in Figure 7b, could be due to this time lag effect.

[38] Second, the $x_m^{\theta_{IMF}}$ shock models are very sensitive to changes in the solar wind conditions when the density is low enough such that $1 < M_A < 2$. For these conditions, changes between the model predictions and observations are amplified because of the $1/M_A^2$ dependence (see, e.g., the shock crossing of Wind at hour 41.5 in Figure 6).

[39] Third, there is also the possibility that time-dependent changes in the shock's shape are important. The shock's shape may not change smoothly to the new equilibrium position as the shock adjusts in a time-dependent fashion. For instance, large-scale time-dependent ripples in the magnetopause structure due to changes in P_{ram} have been reported in simulations [e.g., Smith, 1991, Figure 5], which could have counterparts in the shock's location and geometry, thereby causing the model predictions to differ significantly from observation.

[40] Fourth, the abundance of helium may also cause changes in the model predictions, since larger values of n_{α}/n_p lead to larger pressure and Mach numbers, thereby reducing the x coordinate of the model predictions. However, these changes are relatively small on the basis of our calculations. Here we have assumed that $n_{\alpha}/n_p = 0.04$, since the helium abundances were not available for all times of the shock crossings. A larger abundance of, say, 10% leads to variations of a few Earth radii in the model predictions. For example, changing n_{α}/n_p to 10% from 4% implies an increase of P_{ram} and M_A by 20% and 10%, respectively. So, for a low M_A shock with $M_A = 2$ and $n_{\alpha}/n_p = 4\%$, M_A becomes 2.2 when $n_{\alpha}/n_p = 10\%$. This implies a decrease in a_s from equation (2) of $\sim 1 R_E$, and the $P_{ram}^{-1/6}$ scaling introduces a further reduction by 2% as well. The total effect is to reduce the original values by only 7%, which results in a displacement of only $\sim 1.6 R_E$ for a low $M_A \sim 2$ shock. As M_A increases, this becomes less important since the models are less sensitive to changes in M_A at high M_A .

[41] Fifth, the simulations of Cairns and Lyon [1995], used to develop the new shock models tested here, represent the magnetopause obstacle using Farris *et al.*'s [1991] mean magnetopause model. This model assumes axial symmetry of the magnetopause and does not contain possible changes in shape and location due to magnetic reconnection [e.g., Farris *et al.*, 1991; Sibeck *et al.*, 1991]. In addition, ring current effects on the magnetopause location are not included [e.g., Formisano *et al.*, 1971]. As suggested by CC2003, the model parameters a_s and $b_{s\phi}$ could be rescaled using a different magnetopause model, similar to those of Verigin *et al.* [2001, 2003] and Fairfield *et al.* [2001]. This has been attempted (plots not shown here). However, there was negligible improvement in the model predictions for $x_m^{\theta_{IMF}}$, and so we suggest using the original unscaled version of the model for simplicity.

8.3. Review of Model Results

[42] Having now discussed the effects that may lead to differences between the model results and observations, we now review the models' performance. The $x_m^{\theta_{IMF}}$ models perform well in predicting the shock's location, with the x_i model performing slightly worse on average. Specifically, out of a total of 29 shock crossings in sections 4–6, 24 were predicted within either 1 hour and/or 5 R_E by the $x_m^{\theta_{IMF}}$ models, and only 21 were predicted by the x_i model. A total of 5 of 29 were not predicted by the model trace actually crossing the spacecraft trajectory but were predicted qualitatively; that is, the model lines moved toward and away from the spacecraft trajectory in the appropriate way (see, e.g., the ISEE 1 crossings between hours 16 and 19 in Figure 2). The $x_m^{\theta_{IMF}}$ models mispredict four shock crossings where there were none observed (three of these are mispredicted by the x_i model also), with a total of five mispredictions for the x_i model. Thus the $x_m^{\theta_{IMF}}$ models perform better than the x_i model: The number of crossings accurately predicted is greater by three, and the number of mispredictions are fewer by one, supporting the use of the CC2003 models. As well as this both elementary theory and MHD simulations demonstrate that the shock's 3-D shape, not just the nose location, should vary strongly with M_A , so it is expected that the $x_m^{\theta_{IMF}}$ models do better than the x_i model. Large differences in the $x_m^{45^\circ}$ and $x_m^{90^\circ}$ models are not

observed in many of the crossings when spacecraft were near the nose of the shock, especially when the x_{sc} coordinates were large (with $|y_{sc}|, |z_{sc}| < 10 R_E$).

[43] The analyses performed on the bow shock database in Figures 8 and 9 demonstrate very good accuracy, on average, for the $x_m^{\theta_{IMF}}$ models. Having a large number of shock crossings allows for a more statistically significant comparison with the models, since some shock behaviors not explicitly included in the models will average out and therefore will not affect the results. For example, problems with the finite propagation speed likely average out, with the data set containing just as many inward moving shocks as outward moving ones. Indeed, the models perform very well in the range $60^\circ < \theta_{IMF} < 140^\circ$ in Figure 8 and $1 < M_A < 10$ for the IMP 8, Magion-4, Cluster, and Geotail spacecraft, with the $x_m^{\theta_{IMF}}$ models predicting the shock position within a few percent on average. This compares very favorably with the case studies in sections 4–6. The x_i model performs significantly worse for the Magion-4 and Cluster data, thereby suggesting that changes in shape (b_s) with M_A are important.

[44] Recently, Merka *et al.* [2003a] compared six bow shock models with IMP 8 data from the bow shock database. Their analysis favored three models in the literature: the models of Formisano [1979], Farris and Russell [1994], and Cairns and Lyon [1995] (equivalent to the x_i model shown here), with each performing equivalently well. The analyses contained in section 7 contain some statistical differences from those of Merka *et al.* [2003a]. Direct comparisons with Figures 5 and 6 of Merka *et al.* [2003a], which contain Cairns and Lyon's [1995] model comparisons, show different trends in the ratio R_{model}/R_{obs} for the $M_A < 4.5$ bin (Figure 5) and the $\theta_{IMF} < 20$ and $\theta_{IMF} > 160$ bins (Figure 6). Where we obtain a ratio $R_{model}/R_{obs} < 1$ and ~ 1 for the low θ_{IMF} and M_A criterion, respectively, Merka *et al.* [2003a] obtain ratios of $R_{model}/R_{obs} > 1$ and < 1 . These statistical differences are due to different sampling of the data as described below.

[45] First, the analyses shown in the paper use the extended IMP 8 database for crossings between 1973 and 2000, whereas Merka *et al.* [2003a] use the IMP 8 data for the period 1973–1999, with crossings observed between 1973–1981 and 1981–1999. Before filtering the data the extended IMP 8 database contains $\sim 11,000$ crossings, whereas the Merka *et al.* [2003a] analysis relied upon ~ 4500 crossings. After removing the ambiguous crossings, Merka *et al.* [2003a] were left with ~ 2300 crossings, whereas the extended database contains ~ 5000 unambiguous crossings. However, after performing the rotation of the crossings to compare with the models and after applying the filters on the upstream conditions as described in section 7, the filtered extended database contains only 10% more crossings than that of the filtered data set in the range 1973–1999 and so does not add any large statistical differences between the two data sets. Moreover, Merka *et al.* [2003c] have redone their analysis using the extended database and showed that their results are qualitatively the same as those of Merka *et al.* [2003a]. Second, as described in section 7, the data were filtered with limits on the upstream parameters v_{sw} , M_A , and M_S (leaving 648 crossings) so that the CC2003 models were applicable. Merka *et al.* [2003a] do not impose similar restrictions on these

parameters (leaving 2293 crossings) but instead bin or filter the data one parameter at a time (see their Figures 4–6). This leads to differences between the analyses here and those of Merka *et al.* [2003a].

[46] One set of filters imposed by Merka *et al.* [2003a] are for the relatively nominal solar wind conditions $M_S > 4.5$, $M_A > 4$, and $45^\circ < \theta_{IMF} < 135^\circ$, for which they obtained a ratio $R_{model}/R_{obs} \sim 0.96 \pm 0.10$ (estimated from Merka *et al.* [2003a, Figure 6]) for Cairns and Lyon's [1995] model. Looking at the plots here with $45^\circ < \theta_{IMF} < 135^\circ$ in Figure 8 and $M_A > 4$ in Figure 9, the average ratios are $\sim 0.99 \pm 0.10$. These are consistent within the errors bars. Moreover, we confirm that we obtain similar trends to the Merka *et al.* [2003a] analyses when redoing the analysis using their filtering. The tendency to overpredict or underpredict the shock location is thus sensitive to the bins or filtering used. We reiterate that the filtering we use is intended to directly test models derived from the simulations of CC2003 which were based upon specific solar wind conditions.

[47] Our analyses here improve significantly, on average, upon Cairns and Lyon's [1995] model, suggesting that the new shock models may also outperform Formisano's [1979] and Farris and Russell's [1994] models (and the three other models tested by Merka *et al.* [2003a]). The $x_m^{\theta_{IMF}}$ models are based upon MHD simulations and so contain the expected theoretical dependencies of shock shape (M_A and ϕ), as well as nose location, upon the upstream solar wind conditions, and so it is expected that the $x_m^{\theta_{IMF}}$ models perform better.

[48] Support for the modeled cross-sectional asymmetries, described by the ϕ dependence of b_s , are shown in Figures 10 and 11. The translated cross section (Figure 10) is qualitatively consistent with CC2003 as well as the observations of Verigin *et al.* [2001] and the analytic bow shock work of Verigin *et al.* [2003]. In addition, the translation of the centroid by $-2.6 R_E$ along z is quantitatively consistent with the $x_m^{\theta_{IMF}}$ models, which predict a translation of ~ 1.8 – $4.8 R_E$ for $2 < M_A < 5$ with $\theta_{IMF} = 45^\circ$ [Chapman *et al.*, 2004; CC2003]. For the elliptical fit in Figure 11 the ratio $L_y/L_z = 0.92$ gives a cross-sectional eccentricity of 0.4 which is consistent with Figure 7 of CC2003 and the 2–7% asymmetries measured by Peredo *et al.* [1995]. Note, however, that the model of Peredo *et al.* [1995] has at least a 20% bias [Merka *et al.*, 2003a]. The shifting of the shock's cross section is difficult to observe in the near-Earth regime, as was seen from the rather similar predictions for the x_i and $m^{\theta_{IMF}}$ models in sections 4–6. The maximum cross-sectional asymmetry for the $x_m^{90^\circ}$ model, for example, occurs at $\epsilon \sim 0.4$ for $M_A \sim 2$ (see CC2003, Figure 7), which corresponds to differences in the extent of the shock in the terminator plane ($x = 0$) of $\sim 4 R_E$. Thus, in the near-Earth regime we can only expect a maximum difference between ϕ -dependent and symmetric paraboloidal models of $\sim 4 R_E$. These differences would be more pronounced farther downstream of Earth.

9. Conclusion

[49] The CC2003 models, for $\theta_{IMF} = 45^\circ$ and 90° , which predict the location of Earth's bow shock based upon MHD simulations, have been tested with observational data. The results show that the models perform well against the data.

Comparisons with Cairns and Lyon's [1995] rotationally symmetric model show that the $x_m^{\theta_{\text{IMF}}}$ models do better on average in locating the shock. The two main features of the model, flaring of the shock and shifting of the shock's cross section for $\theta_{\text{IMF}} = 45^\circ$ due to dependences of the shock shape on M_A , azimuthal angle ϕ , and θ_{IMF} , are both supported.

[50] **Acknowledgments.** This work was supported by the Australian Research Council and NASA grant NAG5-6369. We gratefully thank Don Fairfield for his advice regarding the shock data analyses as well as for supplying us with IDL code relevant for the work in sections 5 and 6. We are grateful to the MIT Space Solar Wind Group for the use of the data in sections 5 and 6. We also thank Justin Kasper for work related to the helium concentrations in the Wind and IMP 8 data.

[51] Shadia Rifai Habbal thanks Jan Merka and another referee for their assistance in evaluating this paper.

References

- Bennett, L., M. G. Kivelson, K. K. Khurana, L. A. Frank, and W. R. Paterson (1997), A model of the Earth's distant bow shock, *J. Geophys. Res.*, **102**, 26,927–26,941.
- Cairns, I. H., and J. G. Lyon (1995), MHD simulations of Earth's bow shock at low Mach numbers: Standoff distances, *J. Geophys. Res.*, **100**, 17,173–17,180.
- Cairns, I. H., D. H. Fairfield, R. R. Anderson, V. E. H. Carlton, K. I. Paularena, and A. J. Lazarus (1995), Unusual locations of the Earth's bow shock on September 24–25, 1987: Mach number effects, *J. Geophys. Res.*, **100**, 47–62.
- Chao, J. K., D. J. Wu, C. H. Lin, Y. H. Yang, X. Y. Wang, M. Kessel, S. H. Chen, and R. P. Lepping (2002), Models for the size and shape of the Earth's magnetopause and bow shock, in *Space Weather Study Using Multipoint Techniques, Proceedings of the COSPAR Colloquium held in Pacific Green Bay, Wanli, Taipei, Taiwan, 27–29 September 2000*, edited by L.-H. Lyu, p. 127, Pergamon, New York.
- Chapman, J. F., and I. H. Cairns (2003), Three-dimensional modeling of Earth's bow shock: Shock shape as a function of Alfvén Mach number, *J. Geophys. Res.*, **108**(A5), 1174, doi:10.1029/2002JA009569.
- Chapman, J. F., I. H. Cairns, J. G. Lyon, and C. R. Boshuizen (2004), MHD simulations of Earth's bow shock: Interplanetary magnetic field orientation effects on shape and position, *J. Geophys. Res.*, **109**, A04215, doi:10.1029/2003JA010235.
- Dmitriev, A. V., J. K. Chao, and D. J. Wu (2003), Comparative study of bow shock models using Wind and Geotail observations, *J. Geophys. Res.*, **108**(A12), 1464, doi:10.1029/2003JA010027.
- Fairfield, D. H. (1971), Average and unusual locations of the Earth's magnetopause and bow shock, *J. Geophys. Res.*, **76**, 6700–6716.
- Fairfield, D. H., I. H. Cairns, M. D. Desch, A. Szabo, A. J. Lazarus, and M. R. Aellig (2001), The location of low Mach number bow shocks at Earth, *J. Geophys. Res.*, **106**, 25,361–25,376.
- Farris, M. H., and C. T. Russell (1994), Determining the standoff distance of the bow shock: Mach number dependence and use of models, *J. Geophys. Res.*, **99**, 17,681–17,689.
- Farris, M. H., S. M. Petrinec, and C. T. Russell (1991), The thickness of the magnetosheath: Constraints on the polytropic index, *Geophys. Res. Lett.*, **18**, 1821–1824.
- Formisano, V. (1979), Orientation and shape of the Earth's bow shock in three dimensions, *Planet. Space Sci.*, **27**, 1151–1161.
- Formisano, V., P. C. Hedgecock, G. Moreno, J. Sear, and D. Bollea (1971), Observations of Earth's bow shock for low Mach numbers, *Planet. Space Sci.*, **19**, 1519–1531.
- Grabbe, C. L., and I. H. Cairns (1995), Analytic MHD theory for Earth's bow shock at low Mach numbers, *J. Geophys. Res.*, **100**, 19,941–19,949.
- Merka, J., A. Szabo, T. W. Narock, J. H. King, K. I. Paularena, and J. D. Richardson (2003a), A comparison with IMP 8 observed bow shock positions with model predictions, *J. Geophys. Res.*, **108**(A2), 1077, doi:10.1029/2002JA009384.
- Merka, J., A. Szabo, J. Šafránková, and Z. Němeček (2003b), Earth's bow shock and magnetopause in the case of a field-aligned upstream flow: Observation and model comparison, *J. Geophys. Res.*, **108**(A7), 1269, doi:10.1029/2002JA009697.
- Merka, J., A. Szabo, J. D. Richardson, and T. W. Narock (2003c), Three decades of bow shock observations by IMP 8 and model predictions, paper presented at Magnetospheric Response to Solar Activity, Charles Univ., Prague, 9–12 Sept.
- Němeček, Z., and J. Šafránková (1991), The Earth's shock and magnetopause position as a result of the solar wind-magnetosphere interaction, *J. Atmos. Terr. Phys.*, **53**, 1049–1054.
- Peredo, M., J. A. Slavin, E. Mazur, and C. A. Curtis (1995), Three-dimensional position and shape of the bow shock and their variation with Alfvénic, sonic, and magnetosonic Mach numbers and the interplanetary magnetic field orientation, *J. Geophys. Res.*, **100**, 7907–7916.
- Shue, J.-H., J. K. Chao, H. C. Fu, C. T. Russell, P. Song, K. K. Khurana, and H. J. Singer (1997), A new functional form to study the solar wind control of the magnetopause size and shape, *J. Geophys. Res.*, **102**, 9497–9512.
- Sibeck, D. G., R. E. Lopez, and E. C. Roelof (1991), Solar wind control of the magnetopause shape, location, and motion, *J. Geophys. Res.*, **96**, 5489–5495.
- Slavin, J. A., and R. E. Holzer (1981), Solar wind flow about the terrestrial planets: 1. Modeling bow shock position and shape, *J. Geophys. Res.*, **86**, 11,401–11,418.
- Smith, M. G. (1991), The magnetopause, *Rev. Geophys.*, **29**, 1008–1016.
- Spreiter, J. R., A. L. Summers, and A. Y. Alksne (1966), Hydromagnetic flow around the magnetosphere, *Planet. Space Sci.*, **14**, 223–253.
- Verigin, M., G. Kotova, A. Slazbo, J. Slavin, T. Gombosi, K. Kabin, F. Shugaev, and A. Kalinchenko (2001), Wind observations of the terrestrial bow shock: 3-D shape and motion, *Earth Planets Space*, **53**, 1001–1009.
- Verigin, M., J. Slavin, A. Szabo, G. Kotova, and T. Gombosi (2003), Planetary bow shocks: Asymptotic MHD Mach cones, *Earth Planets Space*, **55**, 33–38.
- Yermoleav, Y. I., and V. V. Stupin (1997), Helium abundance and dynamics in different types of solar wind streams: The Prognos 7 observations, *J. Geophys. Res.*, **102**, 2125–2136.

I. H. Cairns and J. F. Chapman, School of Physics, University of Sydney, Sydney, NSW 2006, Australia. (cairns@physics.usyd.edu.au; jchapman@physics.usyd.edu.au)